

Available online at www.sciencedirect.com

jmr&t
Journal of Materials Research and Technology

journal homepage: www.elsevier.com/locate/jmrt

Original Article

The influence of laser directed energy deposition (DED) processing parameters for Al5083 studied by central composite design



David Svetlizky^a, Baolong Zheng^b, David M. Steinberg^c,
Julie M. Schoenung^b, Enrique J. Lavernia^b, Noam Eliaz^{a,*}

^a Department of Materials Science and Engineering, Tel-Aviv University, Ramat Aviv, Tel Aviv, 6997801, Israel

^b Department of Materials Science and Engineering, University of California, Irvine, Irvine, CA, 92697-2575, USA

^c Department of Statistics and Operations Research, School of Mathematical Sciences, Tel-Aviv University, Ramat Aviv, Tel Aviv, 6997801, Israel

ARTICLE INFO

Article history:

Received 14 January 2022

Accepted 7 February 2022

Available online 14 February 2022

Keywords:

Additive manufacturing (AM)
Directed energy deposition (DED)
Laser Engineered Net Shaping (LENS®)
Aluminum alloys
Central composite design (CCD)
Response surface methodology (RSM)

ABSTRACT

Laser directed energy deposition (DED) of high-quality structural Al-based alloys is challenging due to the inherent physical and thermal properties of the Al powder feedstock. Therefore, an in-depth understanding of the influence of the applied processing parameters on the characteristics of the deposited material is paramount if one is to attain optimal performance. The objective of this study is to investigate the influence of the dominant processing parameters (laser power, scan speed, powder mass flow rate (PMFR), and hatch spacing) on the geometrical characteristics (track's height and dilution) of Al5083 double tracks fabricated using Laser Engineered Net Shaping (LENS®). Central composite design (CCD) response surface methodology (RSM) was utilized to study the influence of the varied processing parameters and their interactions and to develop an empirical statistical prediction model for the studied responses. The results reveal that the applied PMFR has a strong influence on the deposited track's height (positive) and dilution (negative). The laser power at the first-order factor shows a weak influence for both studied responses. However, the interaction between the laser power and the hatch spacing shows significant effects on the track's height and dilution. The microstructure and microhardness of the as-deposited Al5083 double tracks are also discussed, as proxies to the anticipated performance of the deposited material.

© 2022 Published by Elsevier B.V. This is an open access article under the CC BY license (<http://creativecommons.org/licenses/by/4.0/>).

1. Introduction

Laser directed energy deposition (DED) is a widely used additive manufacturing (AM) process. It utilizes the unique set of

interactions between a focused laser beam, the delivered feedstock material (powder or wire), and the formed melt pool. Upon melt pool solidification, near-net-shape parts are built layer-by-layer according to a pre-defined three-dimensional (3D) computer-aided design. The DED process is not

* Corresponding author.

E-mail address: neliaz@tau.ac.il (N. Eliaz).

<https://doi.org/10.1016/j.jmrt.2022.02.042>

2238-7854/© 2022 Published by Elsevier B.V. This is an open access article under the CC BY license (<http://creativecommons.org/licenses/by/4.0/>).

limited solely to the deposition of 3D parts; it also has some attractive cladding [1,2] and repair [3] applications. The complex inherent process characteristics of the DED process, such as repeated heating-cooling thermal cycles, rapid solidification, and laser beam/delivered powder/melt pool interactions, have a direct effect on the properties of the deposited material. The ability to control the abovementioned process characteristics is a key for achieving a defect-free material with desirable microstructure and optimal properties [1,4,5].

Aluminum alloys have gained popularity over the last decades due to their exceptional combination of physical and mechanical properties, such as high specific strength, excellent corrosion resistance, good ductility, and low recyclability costs [6]. Hence, Al alloys are widely utilized in numerous applications and industries; automotive, aerospace, marine, defense, and biomedical, among others [7,8]. The increased interest and need by high-impact industries for alternative processing technologies that allow Al alloy fabrication with geometrical flexibility, increased design freedom, and enhanced properties have driven the AM community. However, to date, AM of useful Al alloys is still considered a significant challenge.

The inherent physical properties of Al, such as high thermal conductivity, high thermal expansion coefficient, oxidation susceptibility, poor powder flowability, low melting temperature, poor melt flowability, and selective evaporation of low-melting alloying elements, make it a significant challenge to utilize laser-based AM, including powder bed fusion (PBF) and DED [9]. The reader is referred to reviews [7,9,10] for a more detailed description of the challenges associated with the fabrication of Al alloys via laser-based AM. The abovementioned characteristics might promote the formation of a variety of defects, such as porosity, lack of fusion (LoF), and cracking [1], thus degrading the mechanical properties of the as-deposited Al alloy.

One of the key barriers that must be overcome in order to successfully deposit a high-quality, defect-free Al alloy with the desired microstructure and enhanced mechanical properties is the establishment of a fundamental understanding of the relations between processing variables and the resulting chemical composition, microstructure, and geometry. For instance, in recent years the study of additively manufactured Al alloys has mainly focused on the deposition of near-eutectic Al–Si and AlSi10Mg hypoeutectic compositions. This is mainly due to the high content of Si, which improves the melt-pool wettability properties and decreases the shrinkage upon rapid solidification [10,11]. In a related study, Kiani et al. [12] successfully established a process window for the deposition of single-track thin walls and 3D blocks by DED of AlSi10Mg. It was shown that the scalability of single-track deposition to thin walls or 3D blocks is limited even when using the same processing parameters. This non-scalability was mainly ascribed to unique thermal history discrepancies associated with the different deposited geometries due to heat accumulation during the increase in deposit's height. This heat accumulation causes a decrease in laser reflectivity and thermal conductivity of Al, thus lowering the applied energy required to enable proper deposition. In AM of Al–Si alloys, selective evaporation of the low melting point alloying elements is not a big issue. On the other hand, in Al–Mg alloys,

selective evaporation of low melting point alloying elements such as Mg and Zn and the low melt wettability pose large barriers. In a recent study, Svetlizky et al. [9] reported a reduction of about 35% in the Mg concentration due to its evaporation in response to the applied laser energy. The effects of the applied process parameters (laser power, laser scan speed, and powder mass flow rate (PMFR)) on the porosity, density, chemical composition, and mechanical properties of the as-deposited alloy were also discussed.

In recent years, many studies have tried to identify, predict, and characterize the influence of the DED key process parameters on the geometry, microstructure, defect formation, thermal history, melt pool shape, and properties of various material systems at the single track, layer, and entire part levels [9,13–22]. However, the high number of involved factors during DED processing (process variables, feedstock-related factors, and deposition system specifications [1]), along with their coupling crosslinking interactions (both synergistic and antagonistic interactions), make the ability to characterize their direct nonlinear influence on the deposit a significant challenge. One way to tackle the challenge is to utilize advanced design of experiments (DOE) and statistical methodologies. Such DOE techniques were reported to be very efficient in: (1) the development of analytical predicting models in terms of input process parameters [18,23], (2) reducing the number of experiments [24], and (3) process optimization [17,25,26].

The central composite design (CCD) methodology allows to embed in the experimental matrix axial and center data points in addition to the full or fractional factorial data points. In a recent report, Guo et al. [26] utilized CCD combined with the analysis of variance (ANOVA) method to develop a prediction model for the effect of the varied DED process parameters on the multilayer geometrical characteristics (width, area, and flatness) of the as-deposited Fe–Cr-based alloy. In addition, the response surface method (RSM) was utilized to obtain the optimal process parameters for a multilayer clad. In another study, Lian et al. [23] established a prediction model to study the effect of critical process parameters (laser power, scan speed, gas flow rate, and overlapping rate) on the clad's geometrical characteristics (width, flatness, and dilution) of M2 tool steel, utilizing both CCD and ANOVA. That study showed an increased deposit width and flatness when applying increased laser power combined with lower laser scan speed and overlap rate, while the gas flow showed an insignificant effect on the deposit width. The latter finding is in good agreement with other studies conducted on various materials [27–29]. In contrast, a combination of reduced laser power and scan speed and increased overlap rate resulted in a reduced dilution. Finally, the optimal process parameters were obtained using the RSM method to attain maximal deposit width with minimal dilution and deposition layer flatness.

To the best of the authors' knowledge, no previous studies have developed a prediction model and investigated the correlation between the key DED processing parameters and the geometrical characteristics of double-track deposition of Al5083. Herein, we employ RSM to develop an analytical prediction model for the combined effects (quadratic and two-way effects) and to evaluate the interactions between the

dominant processing parameters (laser power, laser scan speed, PMFR, and hatch spacing) and the deposited Al5083 geometrical characteristics responses.

2. Methodology

2.1. Materials and deposition of double tracks

A pre-alloyed gas atomized Al5083 powder synthesized by TLS Technik GmbH & Co. (Bitterfeld-Wolfen, Germany) was used as a feedstock material. The chemical composition of the powder was: 4.527 wt.% Mg, 0.544 wt.% Mn, 0.242 wt.% Fe, 0.027 wt.% Zn, 0.006 wt.% Ti, 0.005 wt.% Cr, 0.004 wt.% Cu, balance – Al. Detailed information on the powder feedstock surface morphology, powder size, and sphericity distribution are given elsewhere [9]. Al6061 plate with a nominal chemical composition of 0.8–1.2 wt.% Mg, 0.4–0.8 wt.% Si, 0.15–0.4 wt.% Cu, 0.04–0.35 wt.% Cr, max 0.7 wt.% Fe, max 0.15 wt.% Mn, max 0.15 wt.% Ti, other elements max 0.15 wt.%, Al – balance, was used as a substrate.

A 750 LENS[®] system (Optomec, Inc., Albuquerque, NM, USA) equipped with continuous-wave 1 kW Nd:YAG laser (IPG Photonics, Inc., Oxford, MA, USA) operated under a controlled environment glove chamber was used to deposit the Al5083 two adjacent single-track depositions (i.e., double tracks) with varied processing parameters conditions. The motivation in analyzing double-track deposits instead of the classical single-track deposition methodology was: (1) to study the influence of the applied hatch spacing on the analyzed dilution and track height, and (2) to evaluate the appropriate hatch spacing value that will result in a flat, defect free “single layer”. The double-track deposition process of the samples was carried out in Ar atmosphere to minimize oxidation during deposition. The O₂ level in the glovebox was maintained below 5 ppm during the deposition process. A 10 min dwell time between two different runs (according to Table 2) was used to allow the substrate to cool down to avoid thermal effects which might influence the measured responses. Only each double-track in a single run was continuous. Furthermore, the gas circulation system was kept on, with shield gas blowing on the substrate during the dwell time. The deposited Al5083 double tracks were sectioned at their center, assuming that their geometry is consistent and uniform along the deposit track. The sectioned samples were mounted and then mechanically grounded using a 320 grit SiC paper. The

Table 1 – DED processing parameters and their corresponding levels.

Factor	Units	Factor Level				
		a	–	0	+	A
Lase power (P)	W	600	675	750	825	900
Powder mass flow rate (m)	g/min	5	10	15	20	25
Laser scan speed (v)	mm/min	700	825	950	1075	1200
Hatch spacing (HS)	mm	0.2	0.3	0.4	0.5	0.6

Table 2 – Central composite design (CCD) experimental matrix with the corresponding response values.

Run	Pattern	Factors				Response	
		P	m	V	HS	H (µm)	D
1	--++	675	10	1075	0.5	7	0.94
2	--+-	675	10	1075	0.3	38.9	0.82
3	A000	900	15	950	0.4	46.8	0.84
4	00A0	750	15	1200	0.4	32.6	0.86
5	----	675	10	825	0.3	29.2	0.86
6	0A00	750	25	950	0.4	164.19	0.57
7	0000	750	15	950	0.4	42.5	0.84
8	0a00	750	5	950	0.4	LoF	1
9	---+	675	10	825	0.5	LoF	1
10	-+-+	675	20	1075	0.3	68.4	0.74
11	+--+	825	10	825	0.5	20.2	0.91
12	+-+-	825	20	825	0.5	92.6	0.70
13	0000	750	15	950	0.4	25.1	0.86
14	000A	750	15	950	0.6	29.9	0.89
15	-+++	675	20	1075	0.5	44.5	0.83
16	+++-	825	20	1075	0.3	70.9	0.75
17	0000	750	15	950	0.4	28.5	0.88
18	00a0	750	15	700	0.4	72.3	0.73
19	000a	750	15	950	0.2	68.7	0.74
20	0000	750	15	950	0.4	38.9	0.84
21	+-+-	825	20	825	0.3	81.6	0.68
22	-+-+	675	20	825	0.3	98.1	0.67
23	+--+	675	20	825	0.5	61.8	0.77
24	+-+-	825	10	825	0.3	34.5	0.86
25	0000	750	15	950	0.4	52.8	0.79
26	+--+	825	10	1075	0.3	19.9	0.91
27	++++	825	20	1075	0.5	63.1	0.78
28	a000	600	15	950	0.4	30.5	0.86
29	0000	750	15	950	0.4	23.9	0.90
30	+--+	825	10	1075	0.5	49.4	0.82

polishing of the ground samples was done using diamond suspensions of 9, 3 and 1 µm abrasive size, while final polishing was done using 0.05 µm silica suspension. Following the final polishing, Keller's reagent (2 mL HF, 3 mL HCl, 5 mL HNO₃, 190 mL deionized (DI) water) was used to chemically etch the samples for macro- and micro-structural characterization. The chemically etched cross-sections were characterized using a light optical microscope (OM) (AX10, ZEISS, Oberkochen, Germany) and a scanning electron microscope (SEM, Quanta 200 FEG, FEI, Waltham, MA, USA). Image analysis software (ImageJ) was used to measure the geometrical characteristics (bead height, cross-sectional deposit area, and melt pool cross-sectional area) of the polished cross-sections of each second track in the double-track depositions. Fig. 1 shows schematics of a double-track deposition with the corresponding analyzed deposition characteristics. The microhardness of the as-deposited double tracks was measured using the Knoop microhardness test under 50 g load applied for 15 s, according to ASTM E384-17.

2.2. Design of experiments (DOE) methodology

In this study, an RSM with a four-factor rotatable CCD experimental design was generated and analyzed using JMP 15.0 data analysis software (SAS Institute Inc., NC, USA). The CCD experimental matrix consisted of 30 double tracks, with 16 factorial points, eight axial points, and six replicated center

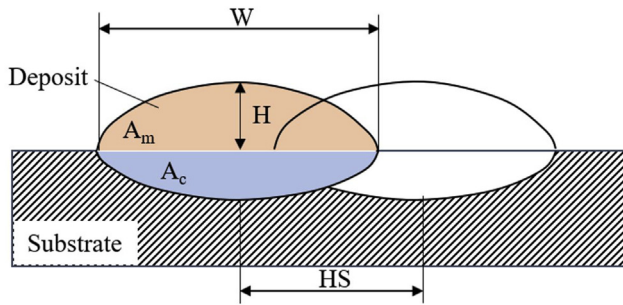


Fig. 1 – Geometrical parameters of double tracks fabricated by DED. W is the deposit's width, H is the deposit's height, HS is the hatch spacing, A_c (colored blue) and A_m (colored orange) are the single track's deposit area and melt pool cross-sectional area, respectively.

point experiments (notated by a four-character pattern of numbers, letters and symbols in Table 2, and marked in red in Figs. 3a,b and 4a,b). The addition of a center–point repetition to a DOE design is an efficient way to evaluate the model's error, validity, and reproducibility [30]. Table 1 lists the variable factors and the corresponding factor levels used for the deposition of Al5083 double-track experimental matrix. The hatch spacing (HS) represents the distance between adjacent deposited single tracks. The track's height (H) and dilution (D) were defined as the model responses. The dilution was calculated using Eq. (1) [31]:

$$D = \frac{A_m}{A_c + A_m} \quad (1)$$

The experimental matrix with the corresponding analyzed response data is shown in Table 2. The implemented RSM allows determining the influence of the applied independent input processing parameters on the output geometrical characteristics and establishing a prediction model for the studied responses. The response prediction model is fitted to the input variables with the following a second-order polynomial equation, Eq. (2) [32]:

$$Y = \beta_0 + \sum_{i=1}^k \beta_i x_i + \sum_{i=1}^{k-1} \sum_{j=i+1}^k \beta_{ij} x_i x_j + \sum_{i=1}^k \beta_{ii} x_i^2 + \varepsilon \quad (2)$$

where Y represents the predicted response variable, x_i and x_j are the independent factors, β_0 , β_i , β_{ij} , and β_{ii} are the model coefficients, and ε is the prediction model error, defined as the independent experimental error.

The RSM analysis was utilized to establish a process parameters map and empirical formula predicting the direct effect and relationship of the studied DED process parameters (Table 1) on the analyzed geometrical characteristics of the as-deposited Al5083 (Table 2) at the studied range of the used factor levels (Table 1). A significance level of less than 5% ($p < 0.05$, t-test) and a lack of fit level $p > 0.05$ (F-test) were used for all statistical analyses. The experimental data were fitted and analyzed in two stages. The first stage included all the effects in Eq. (2) and normalized versions of the factors. Then, non-significant effects were eliminated according to the defined significance criteria of their effects on all studied

responses. In the case of effect heredity, first-order effects were retained even if not passing the model significance criteria if the factor was involved in a second-order effect. The resulting reduced model was fitted in the second stage without normalizing the factors.

3. Results and discussion

Al5083 double tracks were successfully deposited by LENS on the Al6061 substrate according to the CCD experimental matrix. The four-factor rotatable CCD experimental matrix and the analyzed responses for each experimental run are shown in Table 2. The DED process involves many variables that directly influence the deposited material microstructure, physical and mechanical properties [1]. The selection of the laser power, scan speed, powder mass flow rate, and hatch spacing as the dominant varying processing parameters in this study was made based on previous experience and the literature [1,33,34].

It should be noted that our model is not ill-posed. The whole point of the CCD is to provide a sufficient basis for estimating all the terms in the second-order polynomial. Removing some of the terms (because they had small effects) does not make the model “more estimable”. As in most model building processes, there is a “bias/variance” tradeoff here: including more terms reduces bias but increases variance (estimating more terms strains the data more, hence higher variance). Those tradeoffs are most glaring in problems that are ill-posed; there (unlike the CCD and second-order model), one cannot fit all terms and, therefore, must apply some form of effect selection or regularization. Even when the model is not ill-posed, the effect selection has a similar impact of inducing regularization, reducing variance, but at the risk of adding bias.

Second-order polynomial regression prediction models for the as-deposited Al5083 double-track geometrical characteristics (height and dilution) were developed in this study using the least-square method, and are presented in Eqs. (3) & (4). The developed prediction models include both quadratic and linear terms.

$$H = 245.553 - 948.333 HS - 0.401 P + 5.2 m + 0.133 v + 0.34 m^2 + 1.164 HS \cdot P - 0.012 m \cdot v \quad (3)$$

$$D = 0.346 + 3.0267 HS + 0.00131 P - 0.0413 m - 0.0005 v - 0.000531 m^2 - 0.00362 HS \cdot P + 0.0000423 m \cdot v \quad (4)$$

Note, Eqs. (3) and (4) are limited to the range of the studied variable factor levels, using input factors with the appropriate units according to Table 1.

Table 3 summarizes the fit and lack-of-fit analyses of the developed empirical prediction models at a 95% level of significance. The summary of fit data assesses the quality of correlation between the predicted and actual measured data using the regression coefficient (R^2). The R^2 of the developed prediction model for the height and dilution responses are 0.88 (Fig. 3a) and 0.89 (Fig. 4a), respectively.

Previous studies suggested that a model fit is considered adequate if the R^2 values are above 0.80 [35,36]. The models

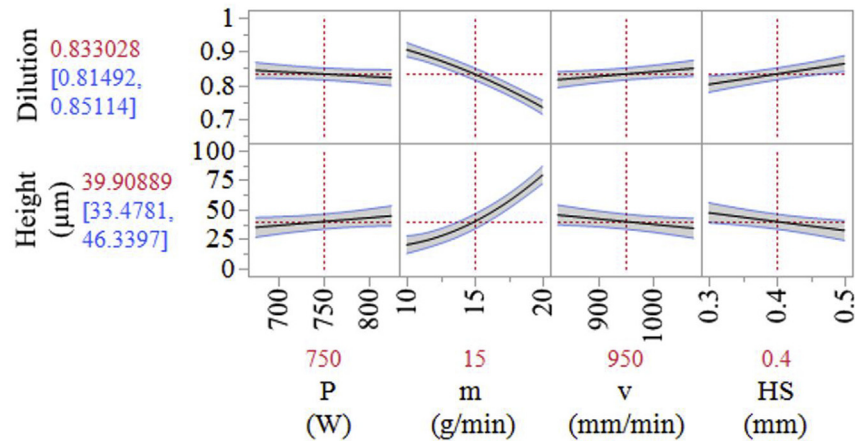


Fig. 2 – A summary of the effects of process parameters on the dilution and height responses at the middle level. The blue envelopes represent the 95% confidence interval of the response.

developed for both height and dilution satisfy this criterion. The adjusted R^2 (adj- R^2 in Table 3) further confirms the validity of the developed models for the studied responses, showing less than 0.05 difference between the adj- R^2 and the obtained R^2 for both response prediction models [37]. The lack-of-fit analysis estimates the validity and accuracy of the developed prediction model based on either the center–point replications (pure error) or the whole model (total error). For both models, the lack-of-fit test found no evidence of the need for more complex prediction equations ($p > 0.05$). Note that the developed response surface prediction model is valid at the factor's levels range (Table 1). However, out of the factors level range, the model might not provide valid prediction, therefore additional data points should be added [38].

According to the developed prediction models, 3D response surface curves were established for each response in order to illustrate the correlations between the independent variable factors and the studied responses at the studied factors' levels. Fig. 2 summarizes the effects on the track's height and dilution responses at the middle levels of each factor.

3.1. Response surface analysis of the deposit's height

At first glance (Table 2), it is evident that a change in the applied processing parameters, including the laser power, scan speed, powder mass flow rate, and hatch spacing, results in a considerable change in the deposit's morphology and geometrical characteristics. Within the range of the studied variable factor levels, the deposited track's height varies between non-successful depositions (defined as LoF, corresponding to $H = 0$) and $164 \mu\text{m}$ (Table 2). Table 4 shows the parameters effect estimation and their significance level considering all linear and quadratic factor interactions influencing the deposit's height response (confidence interval marked between vertical blue dashed lines). Table 4 also displays the type of parameter effect (negative or positive) on the deposit's height response. The analyzed p -value of the laser power factor is 0.0834, i.e., not passing the defined significance level ($p < 0.05$). However, the interaction between the laser power and the hatch spacing ($P \times HS$) is significant. Hence, due

to the hierarchy principle, the laser power factor should not be eliminated from the prediction model of the deposit's height. Among the six parameters which passed the significance test, the powder mass flow rate (first- and second-order) exhibits the most significant effect on the deposit's height.

Fig. 3a shows the correlation between the actual and predicted deposited track's height data of the developed RSM prediction model. Fig. 3b shows the residuals from the fit to the deposit's height in relation to the predicted fit model. The residual plot presents a random distribution of the residuals around the fitted model, serving as an additional confirmation that there is a good agreement between the actual measured Al5083 deposit's height and the developed predictive model [39]. Fig. 3c–f presents the 3D response surfaces that show the influence of the variable factors on the deposit's height prediction at various factor combinations. Mapping the deposit's height, it becomes apparent that the deposit's height was maximized by setting the powder mass flow rate to the highest level while keeping the other variable factors at the center point (notated by the pattern: 0 A 0 0, see Table 2). Fig. 3c–f illustrates the significant positive effect of the powder mass flow rate on the deposit's height. This observation is in good agreement with recent studies [15,39,40] showing a similar trend. By considering suitable laser power and scan speed, increasing the powder mass flow rate enables more feedstock powder to be incorporated and absorbed in the melt pool, thus resulting in an increased deposit's height. At the same time, the laser scan speed and hatch spacing show a negative effect on the deposit's height. These behaviors can be explained by the interaction between the applied laser beam, feedstock powder, and the formed melt pool. As the laser scan speed increases, both the laser energy density and the powder density (g/mm^2) are decreased. The residence time of the laser per introduced powder is also decreased, reducing the amount of feedstock powder absorbed into the formed melt pool, and consequently resulting in a reduced deposit's height.

Fig. 3c and d shows that the laser power has a positive effect on the track's height. This observation is consistent with previous studies showing that the increase in laser power leads to a significant increase in the width and penetration

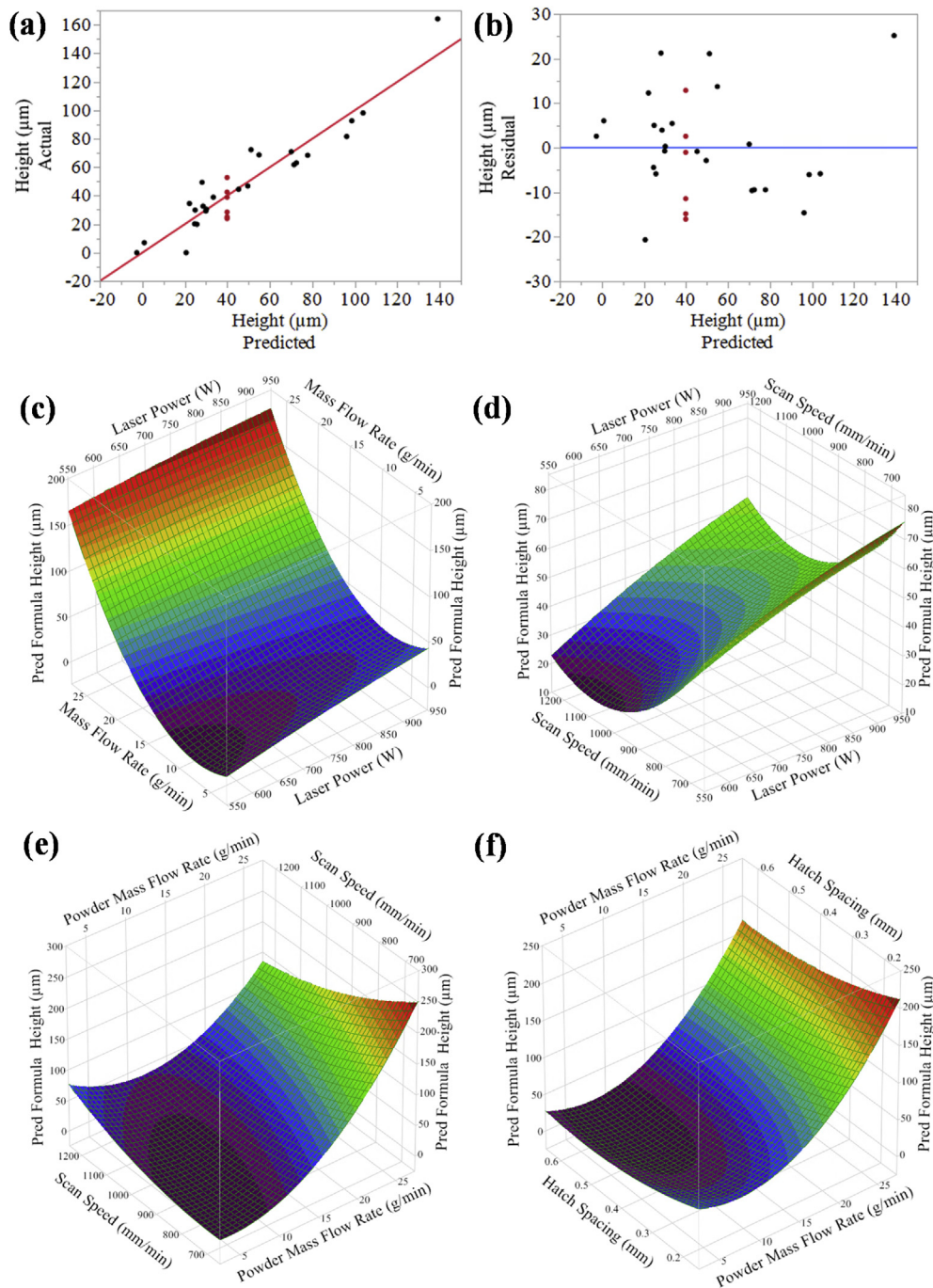


Fig. 3 – (a) Comparison between the predicted and actual data for the height response. (b) A residuals plot of the track's height. Response surface plots showing the predicted track's height as a function of (c) laser power and powder mass flow rate, (d) laser power and scan speed, (e) powder mass flow rate and scan speed, (f) powder mass flow rate and hatch spacing.

depth dimensions of the melt pool [41,42] as well as increase in the deposit's height and width [42–44]. However, as evident from Table 4 and Fig. 3c,d, the effect of laser power is much weaker in comparison to the other parameters included in the prediction model (e.g. powder mass flow rate). To be able to justify such an effect, especially at the single-layer regime, the physical properties of the feedstock Al and the Al substrate should be considered. Physical properties such as the high

reflectivity of the aluminum feedstock and substrate, along with the high thermal conductivity of the Al substrate, result in a lower amount of laser energy being absorbed, and consequently – in a smaller melt pool compared to a material with lower thermal conductivity and laser reflectivity. Hence, a reduced amount of powder is able to be incorporated and absorbed in the formed molten pool, thus leading to the formation of a deposit with a reduced height. Furthermore,

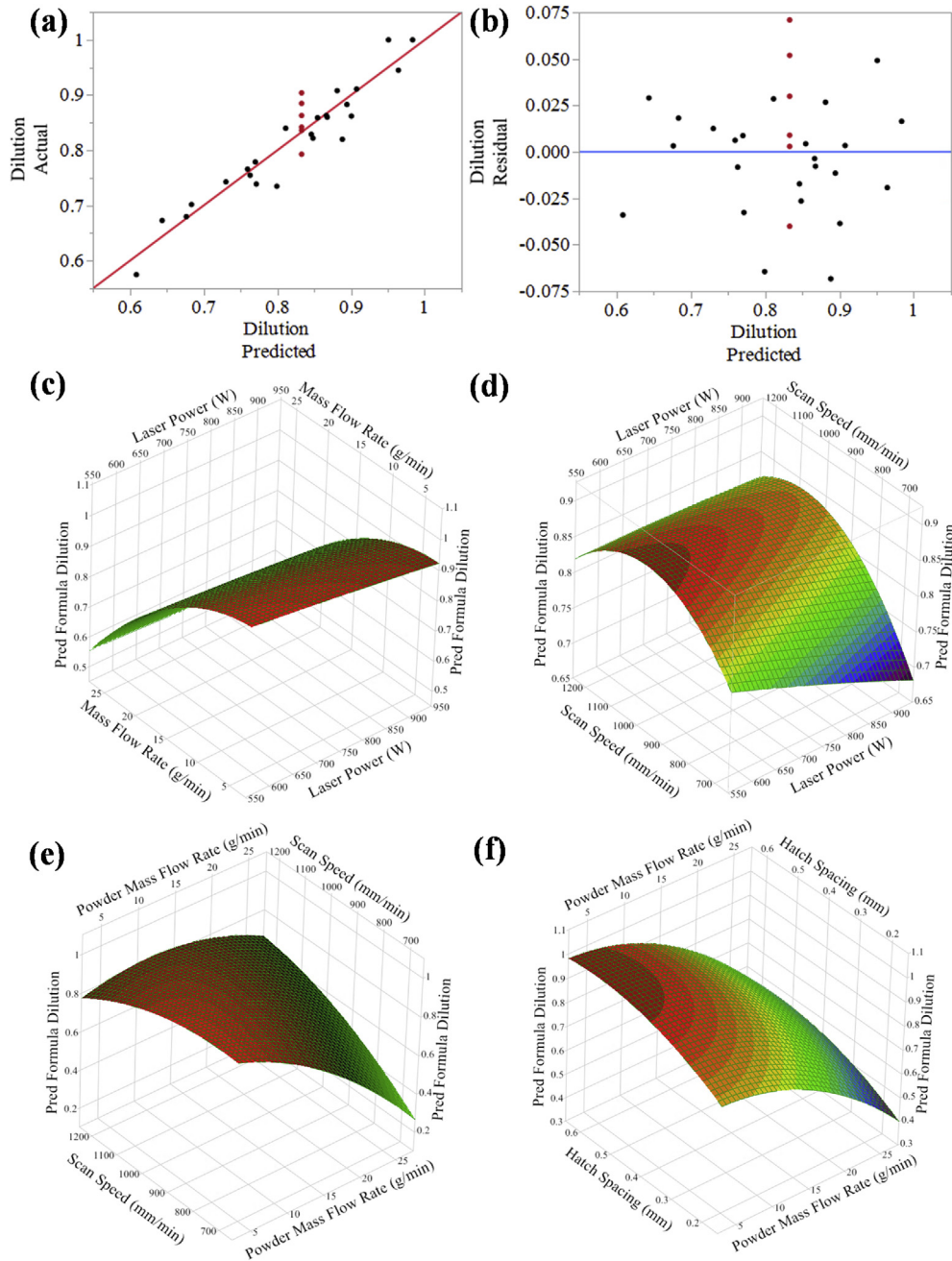


Fig. 4 – (a) Comparison between the predicted and actual data for the dilution response. (b) A residuals plot of the dilution. Response surface plots showing the predicted dilution as a function of (c) laser power and powder mass flow rate, (d) laser power and scan speed, (e) powder mass flow rate and scan speed, and (f) powder mass flow rate and hatch spacing.

Table 3 – Summary of fit and lack-of-fit analyses.

Source	DF	Sum of Squares	Mean Square	F-Ratio
<i>Height</i> , $R^2 = 0.88$, $Adj-R^2 = 0.84$, Root Mean Square error = 13.16				
Lack of fit	17	3156.43	185.67	1.42
Pure error	5	651.29	130.26	Prob > F
Total error	22	3807.72	0.37	
<i>Dilution</i> , $R^2 = 0.89$, $Adj-R^2 = 0.85$, Root Mean Square error = 0.037				
Lack of fit	17	0.022	0.0013	0.85
Pure error	5	0.0077	0.0015	Prob > F
Total error	22	0.030	0.63	

Table 4 – The effect of different variables on the deposit's height.

Term	Estimate	Std Error	t- Ratio	Prob <t
m (g/min)	29.595	2.685442	11.02	<0.0001 ^a
$m \times m$ (g ² /min ²)	9.9801389	2.451462	4.07	0.0005 ^a
HS (mm)	-7.520833	2.685442	-2.80	0.0104 ^a
P (W) \times HS (mm)	8.73125	3.288981	2.65	0.0145 ^a
m (g/min) $\times v$ (mm/min)	-7.40625	3.288981	-2.25	0.0346 ^a
v (mm/min)	-5.6375	2.685442	-2.10	0.0475 ^a
P (W)	4.8708333	2.685442	1.81	0.0834

^a Denotes a statistically significant value.

insufficient laser power may also result in an inability to properly melt all incorporated powder, also resulting in a reduced deposit's height.

The distance between two adjacent deposition tracks, i.e., the hatch spacing, is a key process parameter that highly influences the geometrical characteristics, dimensional accuracy, and defect formation in DED deposition of multilayer structures [4,40]. Most commonly, when discussing the influence of hatch spacing on the deposit's height, studies have mainly focused on the height in the single/multi-layer level to achieve either a minimal flatness ratio [45] or dimensional accuracy [46]. There is limited information in the literature on the influence of the hatch spacing on the geometrical characteristics in the context of the influence on the adjacent deposited single-track's height. The adjacent track geometrical characteristics are influenced by the previous track geometrical characteristics (e.g., height, width, contact angle), surface roughness, and the hatch spacing [47]. Interestingly, the hatch spacing factor exhibited in this study a negative effect on the deposit's height (see Table 4). Fig. 3f shows that the increase in the hatch spacing leads to the formation of deposits with a slight reduction in height. This observation is not consistent with a previous study that showed noncoherent trends for both the adjacent deposit width and height as the applied hatch spacing was increased [48]. However, it should be noted that the material system, laser type, and processing parameters utilized in Ref. 48 were different from those used in the current study.

3.2. Response surface analysis of the dilution

The DED process utilizes a focused high-energy laser to form a melt pool on the substrate while introducing material feedstock powder into the melt pool. Upon the laser's movement, rapid solidification of the melt pool takes place to form a deposit track. One of the key principles of material deposition using DED is establishing sufficient metallurgical bonding between the deposited material and the substrate/previous deposited layer. Dilution is often used to quantify the metallurgical bonding level, and is expressed according to Eq. (1). Previous studies established a general standard defining an optimal range of 10–30% dilution for optimal metallurgical bonding [49,50].

Within the range of the studied variable factor levels, the obtained dilution varied between 1 for unsuccessful

depositions (LoF) and 0.54 (Table 2). The dilution obtained in this study thus has relatively high values. This may be related to the inherent challenge in deposition of Al alloys by DED. The high reflectivity of the Al substrate and the injected Al powder requires a substantial amount of energy to form a proper melt pool as most of the applied laser energy is reflected by the Al substrate instead of being absorbed. This leads to increased melt pool dimensions, and consequently, increased penetration area and relatively shallow deposits (Table 2), altogether leading to increased dilution values.

Table 5 shows the parameters effect estimation and their significance level, considering all linear and quadratic factor interactions that influence the dilution response. The type of parameter effect (negative or positive) on the dilution response is also presented (Table 5). As can be seen in Table 5, the second-order parameter of the powder mass flow rate is insignificant ($p > 0.05$); hence, it was excluded from the analyzed dilution prediction model. Among the significant parameters, the powder mass flow rate shows the most significant effect on the dilution response (negative effect). This could be expected, as an increased powder mass flow rate leads to an increase in the deposition area (A_c), thus reducing the dilution value.

Fig. 4a shows the correlation between the actual and predicted dilution of the developed RSM prediction model. Fig. 4b shows the dilution distribution of the residuals data points in relation to the predicted fit model. The residuals plot presents a random distribution of the residuals around the fit model, with a good agreement between the actual and predicted dilution. The effect of the applied powder mass flow rate can be observed in the response surface plots shown in Fig. 4c–f. As can be seen in Fig. 4d, the increase in laser scan speed has an opposite effect; it results in a reduced deposit track area while having a negligible effect on the penetration area, thus leading to the observed increased dilution.

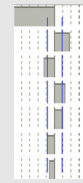
The laser power exhibits only a minor positive effect on the obtained dilution (Fig. 4c,d). The analyzed p -value of the laser power factor is 0.1676, not passing the defined significance level ($p < 0.05$). Yet, the interaction between the laser power and the hatch spacing ($P \times HS$) is significant. Hence, due to the hierarchy principle, the laser power factor was not eliminated from the prediction model of the dilution.

The significant effect of an increase in the applied laser power on the observed dilution could be expected as it directly increases the melt pool area. However, the increase in laser

Table 5 – The effect of different variables on the deposit's dilution.

Term	Estimate	Std Error	t-Ratio	Prob <t
m (g/min)	− 0.085458	0.007563	−11.30	<0.0001 ^a
HS (mm)	0.0307083	0.007563	4.06	0.0005 ^a
P (W) \times HS (mm)	− 0.027188	0.009262	− 2.94	0.0077 ^a
m (g/min) $\times v$ (mm/min)	0.0264375	0.009262	2.85	0.0092 ^a
v (mm/min)	0.0167917	0.007563	2.22	0.0370 ^a
$m \times m$ (g ² /min ²)	− 0.013285	0.006904	− 1.92	0.0673
P (W)	− 0.010792	0.007563	− 1.43	0.1676

^a Denotes a statistically significant value.



power also positively affects the deposit area, as more introduced powder particles are melted. Therefore, the laser power effect on the dilution is mainly controlled by the strength of the laser power effect on both the deposit and penetration areas, as both compensate each other according to Eq. (1), resulting in an only minor effect on the dilution [51].

In DED processing of both single-layer coating deposits and 3D items, the hatch spacing plays a vital role in controlling defects such as interlayer porosity, cracking, and surface roughness [52]. In this study, two adjacent tracks were deposited with a pre-defined hatch spacing, according to the range of levels presented in Table 1. The first track was deposited on the Al 6061 substrate, while the adjacent second track was deposited partly on a previously deposited track. As shown in Table 5, the hatch spacing factor displays a statistically significant positive effect ($p < 0.05$) on the dilution response at the level of the studied factors. However, the positive effect of the HS on the dilution becomes weaker as the P is increased. As the hatch spacing value increases, the obtained deposited area (A_c) is decreased, leading to an increase in the deposit dilution (Fig. 4f). This observation is in good agreement with previous reports [52]. It should be borne in mind that the partial pressure of oxygen affects surface tension, and thereby the behavior of the molten “bead”. Here, we used an Optomec system, which allowed us to maintain the O_2 level in the glovebox constantly and repeatedly at below 5 ppm during the deposition process. Table 6 compares the relationships between the substrate and powder chemistries, processing parameters, O_2 level, and the responses (deposit's height and dilution), as previously reported. It is evident that in most cases a shielding gas was used (although a few publications report O_2 levels lower than either 20 ppm or 5 ppm), which typically cannot ascertain similar low levels of oxygen and repeatability.

3.3. Double-track characterization

3.3.1. Microstructure

The macrostructure and microstructure of the DED deposited double tracks were characterized using OM and SEM. Both transverse and longitudinal cross-sections were studied. Fig. 5.a shows a low-magnification top view of a representative double-track deposition (Run 21, pattern: + + −). In general, most of the studied double tracks showed continuous and uniform track morphology, if neglecting the

unsuccessful depositions (Runs 8 and 9). However, as can be seen in Fig. 5a, a non-uniform surface with numerous partly melted powder particles attached is apparent on the double-track surface and the substrate adjacent to it. Haley et al. [59] ascribed this phenomenon to feedstock particles that either float on the melt pool surface and freeze at the melt pool boundaries, where a lower temperature exists, or melted feedstock particles that pass through the laser beam path, forming a molten droplet which falls and solidifies on the surface. Fig. 5b shows the microstructure at the cross-section of the double track presented in Fig. 5a. The boundaries of the double-track deposit can clearly be seen, forming a mesh-like morphology [9]. The sequence of deposits is also clear, as the second track (left solidification cell) is at a hatch spacing distance to the first track (right solidification cell) and partly re-melts the adjacent deposited track. Fig. 5c,d reveals distinct microstructures at the top and bottom of a single solidification cell cross-section, composed of a selectively etched phase surrounded by the α -aluminum. The secondary phase is comprised of a mixture of lamellar and rod-like eutectic structures, which are commonly related to unsteady/rapid rate solidification [60]. The volume fraction of the rod and lamellar morphologies is controlled by the cooling rate; the volume fraction of the rod phase increases with solidification velocity [61]. The selectively etched phase is assumed to be Mg-rich based on the chemical composition of the deposited Al5083 feedstock and our previous study [9]. However, due to the nature of the melt pool dynamics during DED processing [62] and the fact that the Al5083 feedstock powder and the Al 6061 substrate have different chemistries, it may also result in a mixture solidification of both constituents.

3.3.2. Microhardness

Knoop microhardness of the as-deposited representative double track (Run 6, pattern: 0 A 0 0) was measured. The mean microhardness of the deposit area (A_c) and the molten pool area (A_m) was 64.4 ± 3.67 KHN and 65.5 ± 2.8 KHN, respectively, showing an insignificant difference between the microhardness of the deposit area and the molten pool area. This lack of difference is ascribed to the turbulent flow of the molten pool during DED deposition due to the Marangoni effect [50,63,64]. The unique flow in the formed melt pool during the deposition process results in the mixing of the Al5083 feedstock powder with the Al 6061 substrate to form a track with uniform

Table 6 – Relationships between substrate and powder chemistries, processing parameters, O₂ level, and the responses (deposit's height and dilution), as previously reported elsewhere. ↑, ↓, ↑↓, –, and NA denote increase, decrease, mixed effect, no effect, and not available, respectively. Abbreviations of statistical analysis methods: RSM – response surface methodology, RA - regression analysis, ANOVA – analysis of variance.

Response	Material		O ₂ level	Processing parameters				Analysis method	Ref.
	Powder	Substrate		<i>m</i>	<i>P</i>	<i>v</i>	HS		
Deposit's height	Al 5083	Al6061	<5 ppm	↑	↑	↓	↓	RSM	Current study
	NiCrAlY	Inconel 738	Shielding gas	↑	↑	↓	NA	RA	[53]
	Monel K500	Monel K500	Shielding gas	↑	↑	↓	↓↑	NA	[48]
	Ti6Al4V	Ti6Al4V	Shielding gas	↑	↑	↓	NA	RA	[28]
	Inconel 718	Ti6Al4V	<20 ppm	NA	–	↓	NA	NA	[54]
	AISI 321 stainless steel	WC-12Co	Shielding gas	↑	↑	↓	NA	RA	[27]
	AISI 420 stainless steel	NiCr–TiC composite	Shielding gas	↑	↑	↓	NA	NA	[43]
	AISI H13	ASTM A36	Shielding gas	↑	↑	↓	NA	RSM	[55]
	Inconel 718	A-286 stainless steel	Shielding gas	↑	↑	↓	NA	RA	[39]
	AlSi10Mg	Al6061	<20 ppm	↑	↑	↓	NA	NA	[12]
	NiCr-chromium carbides	Titanium aluminide	Shielding gas	↑	↑	↓	NA	RA	[56]
	NiCr-alloy (19E)	C45 low-alloyed steel	NA	↑	–	↓	NA	RA	[57]
	Ti6Al4V	Ti6Al4V	Shielding gas	↑	↓↑	↓	NA	ANOVA, RSM	[58]
	Dilution	Al 5083	Al6061	<5 ppm	↓	–	↑	↑	RSM
NiCrAlY		Inconel 738	Shielding gas	↓	–	↑	NA	RA	[53]
Ti6Al4V		Ti6Al4V	Shielding gas	↓	–	↑	NA	RA	[28]
AISI 321 stainless steel		WC-12Co	Shielding gas	↓	↑	↑	NA	RA	[27]
AISI 420 stainless steel		NiCr–TiC composite	Shielding gas	↓	↑	↓	NA	NA	[43]
Inconel 718		A-286 stainless steel	Shielding gas	↓	↓	↑	NA	RA	[39]
NiCr-chromium carbides		Titanium aluminide	Shielding gas	↓	–	↑	NA	RA	[57]
NiCr-alloy powder (19E)		C45 low-alloyed steel	NA	↓	↑	↑	NA	RA	[57]
Ti6Al4V	Ti6Al4V	Shielding gas	↓	↑↓	↓	NA	ANOVA, RSM	[58]	

hardness within a single solidification cell. Discrete Knoop microhardness measurements of a vertical scan line (from the top of the deposit to the substrate) of a representative double

track are shown in Fig. 6. The gradual increase in microhardness at the substrate zone is ascribed to the thermal changes that the base material undergoes due to the exposure

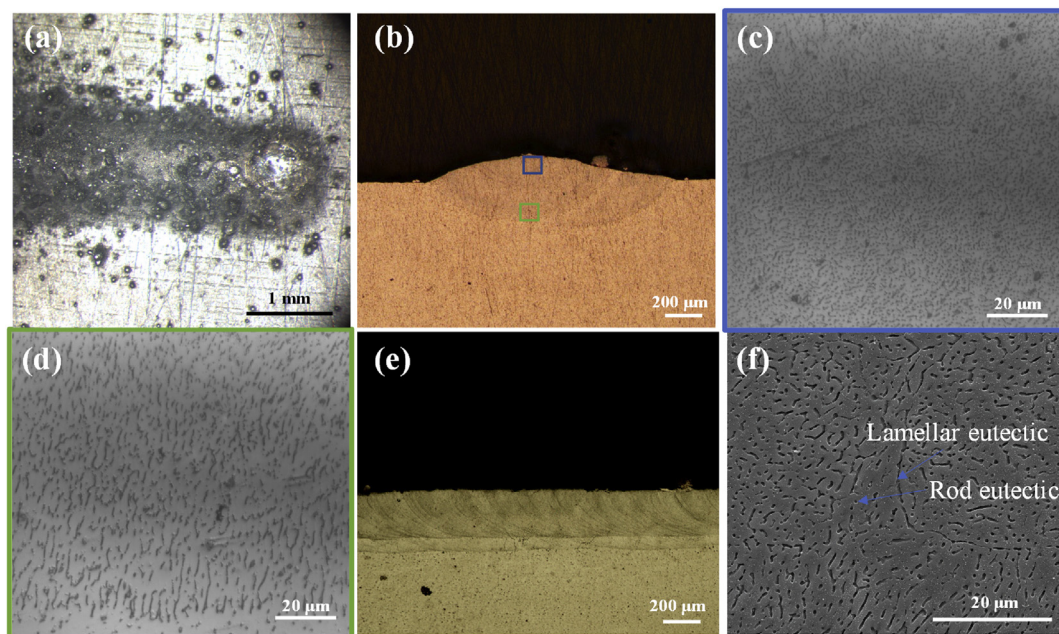


Fig. 5 – Micrographs showing the macro/micro-structure of a DED Al5083 double track on Al6061 substrate (Run 21, pattern: + + – –). (a) Light stereomicroscopy top view. (b) Cross-section OM image after chemical etching. The blue and green rectangles correspond to the zoom-in images shown in (c) and (d), respectively. (c) OM zoom-in image of the blue rectangle zone in (b). (d) OM zoom-in image of the green rectangle zone in (b). (e) OM and (f) SEM images of a longitudinal cross-section.

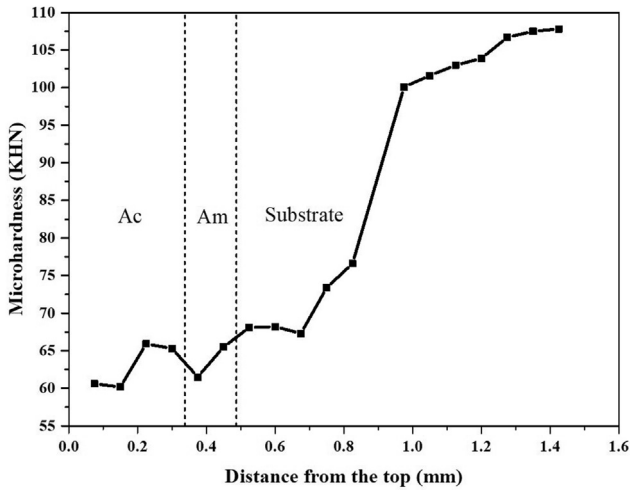


Fig. 6 – Knoop microhardness discrete vertical line scan measurements from the top to the substrate on the as-deposited double-track cross-section (Run 6, pattern: 0 A 0 0).

to increased temperature during the deposition process (heat-affected zone, HAZ).

3.3.3. Defects

DED is associated with various complex out-of-equilibrium processes affected by the rapid cooling rates 10^2 – 10^4 K/s [65], extreme thermal gradients 10^4 – 10^5 K/m [66], and various laser-feedstock-melt pool interactions [1]. DED deposits may

contain various types of defects [1] in their as-deposited state, which influence their physical and mechanical properties. The formation of defects during the DED processing is governed by the applied process parameters (applied energy density (J/mm^2), powder density (g/mm^2), hatch spacing, etc.), and the deposited feedstock properties (density, laser reflectivity, thermal conductivity, melting temperature, selective evaporation, etc.). The understanding of the underlying effects of the applied processing parameters on the deposited material and the interactions between the processing parameters is vital for the fabrication of defect-free material using the DED process.

Fig. 7 presents the most common defects in the double tracks. Fig. 7a,b shows interlayer porosity between the two adjacent tracks. In general, interlayer porosity is a common defect in DED-processed parts [1]; it is usually associated with spherical pores that are located mainly between adjacent tracks and layers that commonly result from insufficient applied energy density, Ar gas entrapment due to the rapid solidification originated in the shielding gas and the powder mass flow rate [9,50]. These are in good agreement with the observations of this study, where interlayer porosity was observed only in Run 6 (pattern 0 A 0 0) associated with the highest powder mass flow rate within the studied powder mass flow rate levels. Recent studies have also reported on the effect of the hatch spacing and overlapping ratio on the formation of intralayer porosity [40,45,67]. These studies showed that an inappropriate selection of the applied hatch spacing between adjacent tracks might result in the formation of voids and incomplete fusion between adjacent tracks and the substrate. In this study, all deposited double tracks showed good metallurgical bonding to the surface, with no

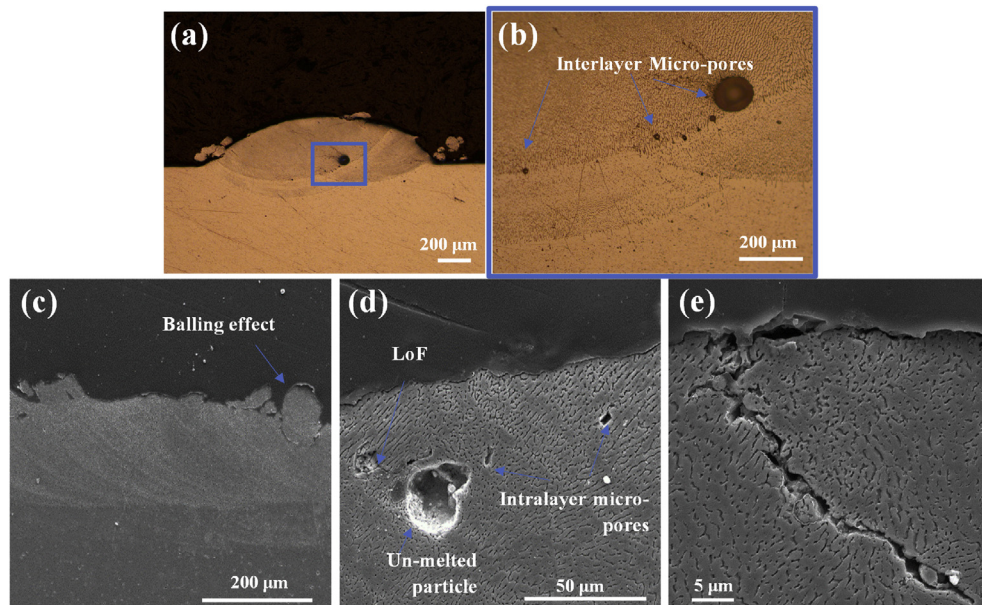


Fig. 7 – Transverse and longitudinal cross-sections, showing different types of defects observed in the DED-deposited Al5083 double tracks. (a) OM image of a transverse cross-section of Run 6 (pattern 0 A 0 0), showing interlayer gas porosity. (b) OM zoom-in image of the blue rectangle zone in (a). (c–e) SEM micrographs of a longitudinal cross-section showing various types of defects observed in Run 22 (pattern: – + – –).

observed voids between the deposit and the substrate. The effect of the applied overlapping ratio between adjacent tracks is not purely geometrical, but also thermal. An increased hatch spacing between adjacent tracks is associated with a larger interface area leading to enhanced heating effect between the two tracks and prolonged melt pool lifetime, and increased melt pool ability to enclose the formed voids [45]. Mitigation of interlayer porosity can be achieved by process optimization and post-processing using hot isostatic pressure (HIP) treatment [1], for example. Fig. 7c–e shows typical defects in a longitudinal cross-section of a representative DED Al5083 double track (Run 22, pattern: – + – –). Balling effect is evident in Fig. 7c. The balling effect is a common defect associated with the DED process leading to increased surface roughness [1]. The formation of balling over the surface of the deposit is mainly associated with the Plateau-Rayleigh instability, resulting in the formation of spherical-like balls at the edges of the surface [4]. However, feedstock particles may also accumulate on the deposit surface due to the ejection of molten droplets out of the melt pool, resulting in spherical particles attached to the deposit's surface. This phenomenon is ascribed to the pressure difference between the melt pool surface tension and the developed recoil pressure in cases where the melt pool temperature exceeds the boiling point of the deposited material [4,68]. Fig. 7d shows intralayer porosity defects commonly associated with DED processing. Such porosity is usually dispersed randomly in the deposited material, and may result from [1]: (1) inherent porosity in the feedstock powder [69]; (2) keyhole phenomenon, originated in localized vaporization in the melt pool due to high applied energy density, forming a cavity which upon solidification results in porosity [70]; (3) LoF, originated due to insufficient applied energy density, resulting in lack of metallurgical bonding between the deposit and the substrate or a previous layer [50], or the presence of native oxides on the surface of the powder feedstock [9]. It should be noted that while keyhole porosity formation is much more likely in laser PBF (L-PBF) than in DED, it has also been reported in DED in general, and in DED of thin layers in particular [71]. Fig. 7e shows an interlayer cracking within the as-deposited Al5083 double track. Cracking is a common challenge of DED parts [1]. The main reason for the formation of such cracks in the as-deposited material is the inherent repetitive heating/cooling cycling and the rapid melt pool solidification, leading to residual stress and, consequently, to cracking of the as-deposited material.

4. Conclusions

In this study, DED of Al5083 double tracks was studied. The effects of the dominant processing parameters (laser power, laser scan speed, powder mass flow rate, and hatch spacing) on the track's height and the dilution were studied by design of experiments (DOE), using central composite design (CCD) and response surface methodology (RSM). Second-order polynomial empirical prediction models correlating the applied processing parameters and the studied responses were developed. The following conclusions were drawn:

1. The as-deposited Al5083 double tracks have good metallurgical bonding to the substrate, with no observed porosity between the deposits and the substrate.
2. All first-order variable factors have a significant effect on the deposit's height and dilution. The powder mass flow rate has the most significant influence on both responses; while increased powder mass flow rate increases the deposit's height, it negatively affects the predicted dilution.
3. The developed track's height prediction model reveals that increasing the powder mass flow rate while reducing the hatch spacing and the scan speed leads to increased deposit's height. The laser power factor at the first order shows a weak influence on the track's height. However, the interaction between the laser power and the hatch spacing shows a significant positive influence on the track's height. Furthermore, the second-order interaction between the applied powder mass flow rate and the scan speed negatively affects the obtained height.
4. The developed track's height prediction model reveals that minimal dilution can be obtained by applying increased powder mass flow rate and laser power while reducing the hatch spacing and scan speed. The laser power factor at the first order shows a weak influence on the track's dilution. However, the second-order interaction between the laser power and the hatch spacing has a significant positive influence on the track's height, while the opposite trend is predicted for the second-order interaction between the powder mass flow rate and the applied scan speed.
5. Microstructural analysis of the double-track deposits reveals an α -aluminum primary phase surrounding a secondary phase comprising a mixture of lamellar and rod-like eutectic structures. Furthermore, the volume fraction of the rod and lamellar morphologies is higher at the top of the track in comparison to the bottom of the track.
6. Only at the maximal level of powder mass flow rate, is an interlayer gas porosity observed.

Credit authorship contribution statement

David Svetlizky: Conceptualization, Methodology, Investigation, Data curation, Writing - original draft, Visualization.
Baolong Zheng: Methodology, Investigation, Writing - review & editing.
Yizhang Zhou: Methodology, Writing - review & editing.
David M. Steinberg: Data analysis, Writing - review & editing.
Julie M. Schoenung: Conceptualization, Methodology, Resources, Writing - review & editing, Supervision, Funding acquisition.
Enrique J. Lavernia: Conceptualization, Methodology, Resources, Writing - review & editing, Supervision, Funding acquisition.
Noam Eliaz: Conceptualization, Methodology, Resources, Data curation, Writing - original draft, Writing - review & editing, Visualization, Supervision, Project administration, Funding acquisition.

Declaration of Competing Interest

The authors declare that they have no known competing financial interests or personal relationships that could have appeared to influence the work reported in this paper.

Acknowledgments

We are grateful to the Israel Ministry of Defense for its financial support: UCI team – under P.O. No. 4440873734, Prof. Eliaz – grant No. 4440783376.

REFERENCES

- [1] Svetlizky D, Das M, Zheng B, Vyatskikh AL, Bose S, Bandyopadhyay A, et al. Directed energy deposition (DED) additive manufacturing: physical characteristics, defects, challenges and applications. *Mater Today* 2021. <https://doi.org/10.1016/j.mattod.2021.03.020>.
- [2] Zhao L, Yue H, Guo C, Li Q, Hao G. Analytical modelling and experimental study of the cladding characteristics of a laser powder-fed additive manufacturing process. *Int J Adv Manuf Technol* 2020;109:2891–900. <https://doi.org/10.1007/s00170-020-05813-w>.
- [3] Balit Y, Guévenoux C, Tanguy A, Upadhyay MV, Charkaluk E, Constantinescu A. High resolution digital image correlation for microstructural strain analysis of a stainless steel repaired by Directed Energy Deposition. *Mater Lett* 2020;270:127632. <https://doi.org/10.1016/j.matlet.2020.127632>.
- [4] DebRoy T, Wei HL, Zuback JS, Mukherjee T, Elmer JW, Milewski JO, et al. Additive manufacturing of metallic components – process, structure and properties. *Prog Mater Sci* 2018;92:112–224. <https://doi.org/10.1016/j.pmatsci.2017.10.001>.
- [5] Shamsaei N, Yadollahi A, Bian L, Thompson SM. An overview of Direct Laser Deposition for additive manufacturing; Part II: mechanical behavior, process parameter optimization and control. *Addit Manuf* 2015;8:12–35. <https://doi.org/10.1016/j.addma.2015.07.002>.
- [6] Black JT, Kohser RA. *DeGarmo's materials and processes in manufacturing*. John Wiley & Sons; 2020, ISBN 978-1-119-49282-5.
- [7] Zhang J, Song B, Wei Q, Bourell D, Shi Y. A review of selective laser melting of aluminum alloys: processing, microstructure, property and developing trends. *J Mater Sci Technol* 2019;35:270–84. <https://doi.org/10.1016/j.jmst.2018.09.004>.
- [8] Aboulkhair NT, Everitt NM, Maskery I, Ashcroft I, Tuck C. Selective laser melting of aluminum alloys. *MRS Bull* 2017;42:311–9. <https://doi.org/10.1557/mrs.2017.63>.
- [9] Svetlizky D, Zheng B, Buta T, Zhou Y, Golan O, Breiman U, et al. Directed energy deposition of Al 5xxx alloy using laser engineered net shaping (LENS®). *Mater Des* 2020;192:108763. <https://doi.org/10.1016/j.matdes.2020.108763>.
- [10] Ding Y, Muñoz-Lerma JA, Trask M, Chou S, Walker A, Brochu M. Microstructure and mechanical property considerations in additive manufacturing of aluminum alloys. *MRS Bull* 2016;41:745–51. <https://doi.org/10.1557/mrs.2016.214>.
- [11] Ye H. An overview of the development of Al-Si-alloy based material for engine applications. *J Mater Eng Perform* 2003;12:288–97. <https://doi.org/10.1361/105994903770343132>.
- [12] Kiani P, Dupuy AD, Ma K, Schoenung JM. Directed energy deposition of AlSi10Mg: single track nonscalability and bulk properties. *Mater Des* 2020;194:108847. <https://doi.org/10.1016/j.matdes.2020.108847>.
- [13] Traxel KD, Malihi D, Starkey K, Bandyopadhyay A. Model-driven directed-energy-deposition process workflow incorporating powder flowrate as key parameter. *Manuf Lett* 2020;25:88–92. <https://doi.org/10.1016/j.mfglet.2020.08.005>.
- [14] Wang G, Sun X, Huang M, Qin Y, Yao Y, Yang S. Influence of processing parameters on the microstructure and tensile property of 85 W-15Ni produced by laser direct deposition. *Int J Refract Metals Hard Mater* 2019;82:227–33. <https://doi.org/10.1016/j.ijrmhm.2019.04.016>.
- [15] Fujishima M, Oda Y, Ashida R, Takezawa K, Kondo M. Study on factors for pores and cladding shape in the deposition processes of Inconel 625 by the directed energy deposition (DED) method. *CIRP J Manuf Sci Technol* 2017;19:200–4. <https://doi.org/10.1016/j.cirpj.2017.04.003>.
- [16] Sun Z, Guo W, Li L. In-process measurement of melt pool cross-sectional geometry and grain orientation in a laser directed energy deposition additive manufacturing process. *Opt Laser Technol* 2020;129:106280. <https://doi.org/10.1016/j.optlastec.2020.106280>.
- [17] Sciammarella F, Salehi Najafabadi B. Processing parameter DOE for 316L using directed energy deposition. *J Manuf Mater Process* 2018;2:61. <https://doi.org/10.3390/jmmp2030061>.
- [18] Saqiba S, Urbanica RJ, Aggarwal K. Analysis of laser cladding bead morphology for developing additive manufacturing travel paths. *Procedia CIRP* 2014;17:824–9. <https://doi.org/10.1016/j.procir.2014.01.098>.
- [19] Riquelme A, Rodrigo P, Escalera-Rodríguez MD, Rams J. Corrosion resistance of Al/SiC laser cladding coatings on AA6082. *Coatings* 2020;10:673. <https://doi.org/10.3390/coatings10070673>.
- [20] Sampson R, Lancaster R, Sutcliffe M, Carswell D, Hauser C, Barras J. The influence of key process parameters on melt pool geometry in direct energy deposition additive manufacturing systems. *Opt Laser Technol* 2021;134:106609. <https://doi.org/10.1016/j.optlastec.2020.106609>.
- [21] Yao Y, Huang Y, Chen B, Tan C, Su Y, Feng J. Influence of processing parameters and heat treatment on the mechanical properties of 18Ni300 manufactured by laser based directed energy deposition. *Opt Laser Technol* 2018;105:171–9. <https://doi.org/10.1016/j.optlastec.2018.03.011>.
- [22] Sreekanth S, Ghassemali E, Hurtig K, Joshi S, Andersson J. Effect of direct energy deposition process parameters on single-track deposits of alloy 718. *Metals* 2020;10:96. <https://doi.org/10.3390/met10010096>.
- [23] Lian G, Yao M, Zhang Y, Chen C. Analysis and prediction on geometric characteristics of multi-track overlapping laser cladding. *Int J Adv Manuf Technol* 2018;97:2397–407. <https://doi.org/10.1007/s00170-018-2107-6>.
- [24] Levi O, Tal B, Hileli S, Shapira A, Benhar I, Grabov P, et al. Optimization of EGFR high positive cell isolation procedure by design of experiments methodology. *Cytom. Part B - Clin Cytom* 2015;88:338–47. <https://doi.org/10.1002/cyto.b.21246>.
- [25] Ansari M, Mohamadizadeh A, Huang Y, Paserin V, Toyserkani E. Laser directed energy deposition of water-atomized iron powder: process optimization and microstructure of single-tracks. *Opt Laser Technol* 2019;112:485–93. <https://doi.org/10.1016/j.optlastec.2018.11.054>.
- [26] Guo C, He S, Yue H, Li Q, Hao G. Prediction modelling and process optimization for forming multi-layer cladding structures with laser directed energy deposition. *Opt Laser Technol* 2021;134:106607. <https://doi.org/10.1016/j.optlastec.2020.106607>.
- [27] Erfanmanesh M, Abdollah-Pour H, Mohammadian-Semnani H, Shoja-Razavi R. An empirical-statistical model for laser cladding of WC-12Co powder on AISI 321 stainless steel. *Opt Laser Technol* 2017;97:180–6. <https://doi.org/10.1016/j.optlastec.2017.06.026>.
- [28] Nabhani M, Razavi RS, Barekat M. An empirical-statistical model for laser cladding of Ti-6Al-4V powder on Ti-6Al-4V

- substrate. *Opt Laser Technol* 2018;100:265–71. <https://doi.org/10.1016/j.optlastec.2017.10.015>.
- [29] Jelvani S, Shoja Razavi R, Barekat M, Dehnavi M. Empirical-statistical modeling and prediction of geometric characteristics for laser-aided direct metal deposition of inconel 718 superalloy. *Met Mater Int* 2020;26:668–81. <https://doi.org/10.1007/s12540-019-00355-7>.
- [30] Usman AI, Aziz AA, Sodipo BK. Application of central composite design for optimization of biosynthesized gold nanoparticles via sonochemical method. *SN Appl Sci* 2019;1:403. <https://doi.org/10.1007/s42452-019-0429-0>.
- [31] Sarathchandra DT, Davidson MJ, Visvanathan G. Parameters effect on SS304 beads deposited by wire arc additive manufacturing. *Mater Manuf Process* 2020;35:852–8. <https://doi.org/10.1080/10426914.2020.1743852>.
- [32] Cavazzuti M. Optimization methods: from theory to design scientific and technological aspects in mechanics. Berlin Heidelberg, Germany: Springer Science & Business Media; 2013. <https://doi.org/10.1007/978-3-642-31187-1>.
- [33] Martukaitz RP. Directed-energy deposition processes. In: Bourell D, Frazier W, Kuhn H, Seifi M, editors. *ASM handbook*, vol. 24. Materials Park, OH: ASM International; 2020. p. 220–38. <https://doi.org/10.31399/asm.hb.v24.9781627082907>. Additive Manufacturing Processes.
- [34] Gibson I, Rosen D, Stucker B. Additive manufacturing technologies. New York, NY: Springer; 2015. p. 245–68. <https://doi.org/10.1007/978-1-4939-2113-3>.
- [35] Joglekar AM, May AT. Product excellence through design of experiments. *Cereal Foods World* 1987;32:857–68.
- [36] Bae IK, Ham HM, Jeong MH, Kim DH, Kim HJ. Simultaneous determination of 15 phenolic compounds and caffeine in teas and mate using RP-HPLC/UV detection: method development and optimization of extraction process. *Food Chem* 2015;172:469–75. <https://doi.org/10.1016/j.foodchem.2014.09.050>.
- [37] Arruda HS, Pereira GA, Pastore GM. Optimization of extraction parameters of total phenolics from annona crassiflora mart. (Araticum) fruits using response surface methodology. *Food Anal Methods* 2017;10:100–10. <https://doi.org/10.1007/s12161-016-0554-y>.
- [38] Erinosh MF, Akinlabi ET. Central composite design on the volume of laser metal deposited Ti6Al4V and Cu. *Mater Tehnol* 2017;51:419–26. <https://doi.org/10.17222/mit.2016.019>.
- [39] Alizadeh-Sh M, Marashi SPH, Ranjbarnodeh E, Shoja-Razavi R, Oliveira JP. Prediction of solidification cracking by an empirical-statistical analysis for laser cladding of Inconel 718 powder on a non-weldable substrate. *Opt Laser Technol* 2020;128:106244. <https://doi.org/10.1016/j.optlastec.2020.106244>.
- [40] Wei HL, Liu FQ, Liao WH, Liu TT. Prediction of spatiotemporal variations of deposit profiles and inter-track voids during laser directed energy deposition. *Addit Manuf* 2020;34:101219. <https://doi.org/10.1016/j.addma.2020.101219>.
- [41] Lee YS, Nordin M, Babu SS, Farson DF. Influence of fluid convection on weld pool formation in laser cladding. *Weld J* 2014;93:292s–300s.
- [42] Feenstra DR, Molotnikov A, Birbilis N. Utilisation of artificial neural networks to rationalise processing windows in directed energy deposition applications. *Mater Des* 2021;198:109342. <https://doi.org/10.1016/j.matdes.2020.109342>.
- [43] Saeedi R, Shoja Razavi R, Bakhshi SR, Erfanmanesh M, Ahmadi Bani A. Optimization and characterization of laser cladding of NiCr and NiCr–TiC composite coatings on AISI 420 stainless steel. *Ceram Int* 2021;47:4097–110. <https://doi.org/10.1016/j.ceramint.2020.09.284>.
- [44] Yu T, Yang L, Zhao Y, Sun J, Li B. Experimental research and multi-response multi-parameter optimization of laser cladding Fe313. *Opt Laser Technol* 2018;108:321–32. <https://doi.org/10.1016/j.optlastec.2018.06.030>.
- [45] Lian G, Zhang H, Zhang Y, Chen C, Huang X, Jiang J. Control and prediction of forming quality in curved surface multi-track laser cladding with curve paths. *Int J Adv Manuf Technol* 2020;106:3669–82.
- [46] Li J, Wang Q, Michaleris P, Reutzel EW. Model prediction for deposition height during a direct metal deposition process. 2017 American Control Conference. Seattle, USA: AACC; 2017. p. 2188–94. <https://doi.org/10.23919/ACC.2017.7963277>.
- [47] Munro C. An empirical model for overlapping bead geometry during laser consolidation. Defence Research and Development Canada, Scientific Report DRDC-RDDC-2019-R007; 2019.
- [48] Munro C. Effect of hatch spacing on bead geometry during blown powder laser additive manufacturing. Defence Research and Development Canada; 2017. Scientific Report DRDC-RDDC-2017-R069.
- [49] Spalding JI. Non-metallic materials processing: an introduction. In: Soares ODD, Perez-Amor M, editors. *Applied laser tooling*. Dordrecht: Nijhoff; 1988. p. 81–93.
- [50] Dass A, Moridi A. State of the art in directed energy deposition: from additive manufacturing to materials design. *Coatings* 2019;9:418. <https://doi.org/10.3390/coatings9070418>.
- [51] Shayanfar P, Daneshmanesh H, Janghorban K. Parameters optimization for laser cladding of inconel 625 on ASTM A592 steel. *J Mater Res Technol* 2020;9:8258–65. <https://doi.org/10.1016/j.jmrt.2020.05.094>.
- [52] Javid Y. Multi-response optimization in laser cladding process of WC powder on Inconel 718. *CIRP J Manuf Sci Technol* 2020;31:406–17. <https://doi.org/10.1016/j.cirpj.2020.07.003>.
- [53] Ansari M, Shoja Razavi R, Barekat M. An empirical-statistical model for coaxial laser cladding of NiCrAlY powder on Inconel 738 superalloy. *Opt Laser Technol* 2016;86:136–44. <https://doi.org/10.1016/j.optlastec.2016.06.014>.
- [54] Corbin DJ, Nassar AR, Reutzel EW, Beese AM, Kistler NA. Effect of directed energy deposition processing parameters on laser deposited Inconel® 718: external morphology. *J Laser Appl* 2017;29:22001. <https://doi.org/10.2351/1.4977476>.
- [55] Farahmand P, Kovacevic R. Parametric study and multi-criteria optimization in laser cladding by a high power direct diode laser. *Lasers Manuf Mater Process* 2014;1:1–20. <https://doi.org/10.1007/s40516-014-0001-0>.
- [56] Aghili SE, Shamanian M. Investigation of powder fed laser cladding of NiCr-chromium carbides single-tracks on titanium aluminide substrate. *Opt Laser Technol* 2019;119:105652. <https://doi.org/10.1016/j.optlastec.2019.105652>.
- [57] de Oliveira U, Ocelík V, De Hosson JTM. Analysis of coaxial laser cladding processing conditions. *Surf Coating Technol* 2005;197:127–36. <https://doi.org/10.1016/j.surfcoat.2004.06.029>.
- [58] Sun Y, Hao M. Statistical analysis and optimization of process parameters in Ti6Al4V laser cladding using Nd:YAG laser. *Opt Laser Eng* 2012;50:985–95. <https://doi.org/10.1016/j.optlaseng.2012.01.018>.
- [59] Haley JC, Schoenung JM, Lavernia EJ. Observations of particle-melt pool impact events in directed energy deposition. *Addit Manuf* 2018;22:368–74. <https://doi.org/10.1016/j.addma.2018.04.028>.
- [60] Verissimo NC, Brito C, Afonso CR, Spinelli JE, Cheung N, Garcia A. Microstructure characterization of a directionally solidified Mg-12wt.%Zn alloy: equiaxed dendrites, eutectic mixture and type/morphology of intermetallics. *Mater Chem Phys* 2018;204:105–31. <https://doi.org/10.1016/j.matchemphys.2017.10.032>.

- [61] Que ZP, Gu JH, Shin JH, Choi HK, Jung YG, Lee JH. Lamellar to rod eutectic transition in the hypereutectic nickel-aluminum alloy. *Mater Today Proc* 2014;1:17–24. <https://doi.org/10.1016/j.matpr.2014.09.004>.
- [62] Zheng B, Haley JC, Yang N, Yee J, Terrassa KW, Zhou Y, et al. On the evolution of microstructure and defect control in 316L SS components fabricated via directed energy deposition. *Mater Sci Eng* 2019;764:138243. <https://doi.org/10.1016/j.msea.2019.138243>.
- [63] Bayat M, Nadimpalli VK, Pedersen DB, Hattel JH. A fundamental investigation of thermo-capillarity in laser powder bed fusion of metals and alloys. *Int J Heat Mass Tran* 2021;166:120766. <https://doi.org/10.1016/j.ijheatmasstransfer.2020.120766>.
- [64] Bayat M, Nadimpalli VK, Biondani FG, Jafarzadeh S, Thorborg J, Tiedje NS, et al. On the role of the powder stream on the heat and fluid flow conditions during Directed Energy Deposition of maraging steel—multiphysics modeling and experimental validation. *Addit Manuf* 2021;43:102021. <https://doi.org/10.1016/j.addma.2021.102021>.
- [65] Manvatkar V, De A, DebRoy T. Heat transfer and material flow during laser assisted multi-layer additive manufacturing. *J Appl Phys* 2014;116:124905. <https://doi.org/10.1063/1.4896751>.
- [66] Griffith M, Schlienger M, Harwell L, Oliver M, Baldwin M, Ensz M, et al. Understanding thermal behavior in the LENS process. *Mater Des* 1999;20:107–13. [https://doi.org/10.1016/S0261-3069\(99\)00016-3](https://doi.org/10.1016/S0261-3069(99)00016-3).
- [67] Lian G, Liu Z, Zhang Y, Feng M, Chen C, Jiang J. The forming control method of multi-track laser cladding on curved surface. *Metals* 2020;10:1109. <https://doi.org/10.3390/met10081109>.
- [68] He X, Norris JT, Fuerschbach PW, DebRoy T. Liquid metal expulsion during laser spot welding of 304 stainless steel. *J Phys D Appl Phys* 2006;39:525–34. <https://doi.org/10.1088/0022-3727/39/3/016>.
- [69] Rabin BH, Smolik GR, Korth GE. Characterization of entrapped gases in rapidly solidified powders. *Mater Sci Eng* 1990;124:1–7. [https://doi.org/10.1016/0921-5093\(90\)90328-Z](https://doi.org/10.1016/0921-5093(90)90328-Z).
- [70] Haley JC, Zheng B, Bertoli US, Dupuy AD, Schoenung JM, Lavernia EJ. Working distance passive stability in laser directed energy deposition additive manufacturing. *Mater Des* 2019;161:86–94. <https://doi.org/10.1016/j.matdes.2018.11.021>.
- [71] Kim K-H, Jung C-H, Jeong D-Y, Hyun S-K. Preventing evaporation products for high-quality metal film in directed energy deposition: a review. *Metals* 2021;11:353. <https://doi.org/10.3390/met11020353>.